(P)RR would require rescue experiments with the WT protein and with mutant proteins that lack the domain responsible for binding renin and prorenin.

Acknowledgments

We thank Shintaro Morizane, Tomohiro Matsuhashi, Shugo Tohyama, Hisayuki Hashimoto, Yoshiko Miyake, and Toshihiro Nagai for excellent technical assistance. We are also grateful to Noboru Mizushima and Genzou Takemura for their comments on the manuscript. Motoaki Sano and Hiroshi Itoh are core members of the Global Center of Excellence (GCOE) for Human Metabolomics Systems Biology, Ministry of Education, Culture, Sports, Science and Technology.

Sources of Funding

This work was supported by a grant from the Ministry of Education, Culture, Sports, Science and Technology (17390249 to A. I.) and a PRESTO (Metabolism and Cellular Function) grant from the Japanese Science and Technology Agency (to M. S.).

Disclosures

None.

References

1. Cruciat CM, Ohkawara B, Acebron SP, Karaulanov E, Reinhard C, Ingelfinger D, Boutros M, Niehrs C. Requirement of prorenin receptor and vacuolar H+-ATPase-mediated acidification for Wnt signaling. *Science*. 2010;327:459–463.
2. Gaussin V, Van de Putte T, Mishina Y, Hanks MC, Zwijsen A, Huylebroeck D, Behringer RR, Schneider MD. Endocardial cushion and myocardial defects after cardiac myocyte-specific conditional deletion of the bone morphogenetic protein receptor ALK3. *Proc Natl Acad Sci U S A*. 2002;99:2878–2883.
3. Sano M, Izumi Y, Helenius K, Asakura M, Rossi DJ, Xie M, Taffet G, Hu L, Pautler RG, Wilson CR, Boudina S, Abel ED, Taegtmeyer H, Scaglia F, Graham BH, Kralli A, Shimizu N, Tanaka H, Makela TP, Schneider MD. Menage-a-trois 1 is critical for the transcriptional function of PPARgamma coactivator 1. *Cell Metab*. 2007;5:129–142.
4. Forgac M. Structure and properties of the coated vesicle (H+)-ATPase. *J Bioenerg Biomembr*. 1992;24:341–350.
5. Sun-Wada GH, Wada Y, Futai M. Vacuolar H+ pumping ATPases in luminal acidic organelles and extracellular compartments: common rotational mechanism and diverse physiological roles. *J Bioenerg Biomembr*. 2003;35:347–358.
6. Supek F, Supekova L, Mandiyan S, Pan YC, Nelson H, Nelson N. A novel accessory subunit for vacuolar H(+)-ATPase from chromaffin granules. *J Biol Chem*. 1994;269:24102–24106.
7. Graham LA, Powell B, Stevens TH. Composition and assembly of the yeast vacuolar H(+)-ATPase complex. *J Exp Biol*. 2000;203:61–70.
8. Hirata R, Umemoto N, Ho MN, Ohya Y, Stevens TH, Anraku Y. VMA12 is essential for assembly of the vacuolar H(+)-ATPase subunits onto the vacuolar membrane in Saccharomyces cerevisiae. *J Biol Chem*. 1993;268:961–967.
9. Ichihara A, Hayashi M, Kaneshiro Y, Suzuki F, Nakagawa T, Tada Y, Koura Y, Nishiyama A, Okada H, Uddin MN, Nabi AH, Ishida Y, Inagami T, Saruta T. Inhibition of diabetic nephropathy by a decoy peptide corresponding to the "handle" region for nonproteolytic activation of prorenin. *J Clin Invest*. 2004;114:1128–1135.
10. Advani A, Kelly DJ, Cox AJ, White KE, Advani SL, Thai K, Connelly KA, Yuen D, Trogadis J, Herzenberg AM, Kuliszewski MA, Leong-Poi H, Gilbert RE. The (Pro)renin receptor: site-specific and functional linkage to the vacuolar H+-ATPase in the kidney. *Hypertension*. 2009;54:261–269.

Novelty and Significance

What is Known?

- (Pro)renin receptor [(P)RR], which plays a key role in the local renin-angiotensin system, is encoded by the *ATP6AP2* gene.
- The gene product of *ATP6AP2* is also associated with V-ATPase, which maintains an acidic environment in the lumen of intracellular vesicular compartments.

What New Information Does This Article Contribute?

- Cardiomyocyte-specific ablation of *Atp6ap2* caused fulminant heart failure.
- Ablation of *Atp6ap2* selectively suppressed protein expression of the V_0 subunits of V-ATPase, resulting in deacidification of intracellular vesicles.
- The phenotypes observed after genetic ablation of *Atp6ap2* are ascribed to V-ATPase loss of function.

The gene products of *ATP6AP2* have 2 distinct functions. Their first role in regulating the renin-angiotensin system pathway is well established, but a secondary role in regulating V-ATPase (and other cellular roles) has not been proposed or investigated in vivo. In the present study, we generated a mouse with a cardiac-specific deficiency in *Atp6ap2*. The *Atp6ap2*-disrupted cardiomyocytes showed extensive vacuolation, a phenotype that could be reproduced by pharmacologically inhibiting intracellular acidification. We demonstrated for the first time that ATP6AP2 might be an essential assembly chaperone of mammalian V-ATPase and that genetic ablation of *Atp6ap2* created a loss-of-function model for V-ATPase.

Downloaded from circres.ahajournals.org at KEIO UNIV IGAKUBU LIB on May 12, 2011

Supplement Material

Full Methods

Animals. All animal experiments were reviewed and approved by the Institutional Animal Care and Use Committee at the Keio University School of Medicine.

Generation of Atp6ap2 conditional knockout mice. The 13.3-kb genomic fragment that contains exons 2 and 3 of the *Atp6ap2* gene was obtained from a mouse BAC clone (RP23-339K2). A targeting vector was designed to insert a *loxP* and *frt*-flanked PGK-*neo* cassette upstream of exon 2, and a third loxP site downstream of exon 2 of the targeted gene. The targeting vector was electroporated into C57/BL6 (B6) mouse-derived embryonic stem (ES) cells. Correctly targeted ES cells were injected into recipient blastocysts, and chimeric mice were bred with C57BL/6 mice, to establish a colony. The mutant mice were then bred with mice that expressed the Flp recombinase, to remove the *frt*-flanked *neo* cassettes. The resulting male *Atp6ap2*flox/Y mice (with loxP sites and a single Frt site remaining upstream of exon 2, and a second loxP site located downstream of exon 2) were bred with female mice that expressed cell-type-specific Cre recombinase.

Cardiomyocyte culture. Neonatal ventricular myocytes from 1- to 2-day-old Sprague-Dawley rats were subjected to Percoll gradient centrifugation and differential plating in order to enrich for cardiac myocytes and deplete nonmyocyte populations.[1]

Histology. Hearts were fixed overnight in 10% formalin at 4°C, dehydrated with 70% ethanol, mounted in paraffin, and sectioned (5-μm thickness). Heart sections were stained with hematoxylin and eosin (HE) or with Masson trichrome for fibrosis.[2] Low and high-magnification fields of short-axis views were analyzed using a BIOREVO (BZ-9000; Keyence, Japan).

For immunostaining, hearts were fixed in 4% paraformaldehyde, then successively infiltrated with 30% sucrose in PBS, embedded in OCT compound (Miles), and stored frozen. Sections of 6 micrometer thickness were mounted on gelatin-coated slides, and then stained with hematoxylin. Sections were stained immunochemically as described previously.[3] The immunnofluorescence of cultured cells were performed as previously described.[4] For the labeling of acidic organelles, cells were incubated with LysoTracker (Molecular Probes) for 30 minutes, and then fixed with 4% paraformaldehyde in PBS (pH 7.4). Fluorescence images were acquired with a confocal microscope, LSM 510 (Carl Zeiss).

For transmission electron microscopy, tissue was minced and fixed in 2% paraformaldehyde, 2.5% glutaraldehyde, and 0.1 M cacodylate buffer, prepared according to standard protocol; and

Downloaded from circres.ahajournals.org at KEIO UNIV IGAKUBU LIB on May 12, 2011

electron microscopy was performed using the RMC MT6000 ultramicrotome, and visualized using the Hitachi H7500 electron microscope and the 2K × 2K Gatan CCD camera.

For sequential time-lapse microscopic analysis, bafilomycin A1-, chloroquine-, or vehicle-treated cardiomyocytes were observed every 20-30minutes over 48-72 hours using Leica FW4000.

Antibodies. Antibodies against V-ATPase a subunits and RAB7 were described previously.[5-8] Other primary antibodies used were monoclonal antibodies for LAMP2 and actin (DSHB and Abcam, respectively), anti-tubulin and GAPDH antibody (Cell Signaling Technology), anti-ATP6AP2 antibody (R&D Systems), anti-p62 C terminus polyclonal antibody (Progen), anti-LC3 (kind gift from Dr. Komatsu, the Tokyo Metropolitan Institute of Medical Science). Fluorescent dye or enzyme-linked secondary antibodies were obtained from Jackson ImmunoResearch.

Gene expression. Total RNA was purified using TRIzol reagent according to manufacturer's instructions. For RT-PCR, total RNA was used for reverse transcriptase using random hexamer primers. Quantitative real-time PCR was performed using the ABI Prism 7700 sequence detection system (Applied Biosystems). Predesigned gene-specific primer and probe sets (TaqMan Gene Expression Assays) were used. The 18s ribosomal RNA was amplified as an internal control.

Western blotting. Protein lysate preparation and immunoblotting procedures were performed as previously described.[9] Total lysates were applied at 10-20 μg/lane on 5-20% gradient polyacrylamide gel (Daiich Pure Chemicals) and transferred to PVDF membrane with 0.2 μm pore size. The immunoblots were performed with aforementioned antibodies. Dulbecco's modified Eagle medium (DMEM), minimal essential medium (MEM) and fetal bovine serum (FBS) were from Invitrogen. The protein blot was developed with an ECL detection kit (GE Healthcare) or chemiluminescence (Amersham Biosciences), and images were obtained using an image capture system (model LAS1000 and LAS3000 luminoimager; Fujifilm). The intensities of bands were measured and analyzed using Image Gauge Software (Fujifilm).

Echocardiography. Mice were anesthetized by inhalation of 1.5% isoflurane, and then immobilized on a positionable platform in the supine position. Short-axis echocardiography and Doppler echocardiographic measurements were made using the Vevo 660 system (VisualSonics) with a 600 series real-time microvisualization scanhead probe.[2] The left ventricular (LV) internal end-systolic diameter and LV end-diastolic diameter (LVESD and LVEDD, respectively) were measured using the leading-edge convention adopted by the American Society of Echocardiography. LV fractional shortening (FS) was calculated according to the formula: FS (%) = [(LVEDD –

Downloaded from circres.ahajournals.org at KEIO UNIV IGAKUBU LIB on May 12, 2011

LVESD)/LVEDD] × 100.

Statistics. Values are presented as mean ± SEM. Statistical significance was evaluated using 2-tailed, unpaired Student's *t* tests for comparisons of 2 mean values. Multiple comparisons involving more than 3 groups were performed using ANOVA. A P value less than 0.05 was considered statistically significant.

Downloaded from circres.ahajournals.org at KEIO UNIV IGAKUBU LIB on May 12, 2011

Online Figure Legends

Online Figure I

Strategy used to generate a conditional *Atp6ap2* allele. The genomic structure, targeting vector, and targeted allele are shown. CDS, coding sequence; UTR, untranslated region; FRT, flipase recognition target.

Online Figure II

Female *Atp6ap2*-floxed mice were bred with male mice that expressed the Cre recombinase under the control of the cardiomyocyte-specific α-myosin heavy chain (αMHC) promoter.

Online Figure III

Ultrastructure of ATP6AP2-depleted cardiomyocytes. **a**, A giant autophagolysosome with undigested cytosolic constituents. **b**, A cytosolic inculusion composed of concentric lamellae body which is often found in lysosomal disease and chloroquine induced cardiomyopathy (arrow) **c**, Mitophagy (arrowhead). Scale bars: 1 μm.

Online Figure IV

a, PCR genotyping of MEF DNA reveals a deletion of floxed *Atp6ap2* contingent on coinheritance of Cre recombinase. **b**, Quantitative PCR analysis reveals ≥90% elimination of *Atp6ap2* from floxed MEFs after Ad-Cre treatment.

Online Figure V

Pharmacologic inhibition of intracellular acidification significantly up-regulates *Atp6ap2* mRNA expression in cultured cardiomyocytes. $*P < 0.05$ vs. WT control (unpaired Student's *t*-test).

Downloaded from circres.ahajournals.org at KEIO UNIV IGAKUBU LIB on May 12, 2011

Online Video Legends

Online Video I

Echocardiographic data in WT (**a**) and cardiomyocyte-specific *Atp6ap2* CKO (**b**) mice on PD18. Echocardiography measurements using left ventricular trace on B-mode images depicts severely impaired ventricular function.

Online Video II

Sequential time-lapse observation of the cultured cardiomyocytes. **a,** Cardiomyocytes treated with vehicle. **b**, Cardiomyocytes treated with bafilomycin A1. **c**, Cardiomyocytes treated with chloroquine. Time scale: 6 hours per second.

Downloaded from circres.ahajournals.org at KEIO UNIV IGAKUBU LIB on May 12, 2011

Supplementary References

1. Tokudome S, Sano M, Shinmura K, Matsuhashi T, Morizane S, Moriyama H, Tamaki K, Hayashida K, Nakanishi H, Yoshikawa N, Shimizu N, Endo J, Katayama T, Murata M, Yuasa S, Kaneda R, Tomita K, Eguchi N, Urade Y, Asano K, Utsunomiya Y, Suzuki T, Taguchi R, Tanaka H, Fukuda K. Glucocorticoid protects rodent hearts from ischemia/reperfusion injury by activating lipocalin-type prostaglandin D synthase-derived PGD2 biosynthesis. *J Clin Invest.* 2009;119:1477-1488.
2. Endo J, Sano M, Katayama T, Hishiki T, Shinmura K, Morizane S, Matsuhashi T, Katsumata Y, Zhang Y, Ito H, Nagahata Y, Marchitti S, Nishimaki K, Wolf AM, Nakanishi H, Hattori F, Vasiliou V, Adachi T, Ohsawa I, Taguchi R, Hirabayashi Y, Ohta S, Suematsu M, Ogawa S, Fukuda K. Metabolic remodeling induced by mitochondrial aldehyde stress stimulates tolerance to oxidative stress in the heart. *Circ Res.* 2009;105:1118-1127.
3. Endo J, Sano M, Fujita J, Hayashida K, Yuasa S, Aoyama N, Takehara Y, Kato O, Makino S, Ogawa S, Fukuda K. Bone marrow derived cells are involved in the pathogenesis of cardiac hypertrophy in response to pressure overload. *Circulation.* 2007;116:1176-1184.
4. Sun-Wada GH, Imai-Senga Y, Yamamoto A, Murata Y, Hirata T, Wada Y, Futai M. A proton pump ATPase with testis-specific E1-subunit isoform required for acrosome acidification. *J Biol Chem.* 2002;277:18098-18105.
5. Nakamura N, Yamamoto A, Wada Y, Futai M. Syntaxin 7 mediates endocytic trafficking to late endosomes. *J Biol Chem.* 2000;275:6523-6529.
6. Toyomura T, Oka T, Yamaguchi C, Wada Y, Futai M. Three subunit a isoforms of mouse vacuolar H(+)-ATPase. Preferential expression of the a3 isoform during osteoclast differentiation. *J Biol Chem.* 2000;275:8760-8765.
7. Nakamura N, Sun-Wada GH, Yamamoto A, Wada Y, Futai M. Association of mouse sorting nexin 1 with early endosomes. *J Biochem.* 2001;130:765-771.
8. Sun-Wada GH, Wada Y, Futai M. Lysosome and lysosome-related organelles responsible for specialized functions in higher organisms, with special emphasis on vacuolar-type proton ATPase. *Cell Struct Funct.* 2003;28:455-463.
9. Sano M, Tokudome S, Shimizu N, Yoshikawa N, Ogawa C, Shirakawa K, Endo J, Katayama T, Yuasa S, Ieda M, Makino S, Hattori F, Tanaka H, Fukuda K. Intramolecular control of protein stability, subnuclear compartmentalization, and coactivator function of peroxisome proliferator-activated receptor gamma coactivator 1alpha. *J Biol Chem.* 2007;282:25970-25980.

Downloaded from circres.ahajournals.org at KEIO UNIV IGAKUBU LIB on May 12, 2011

Online Figure I

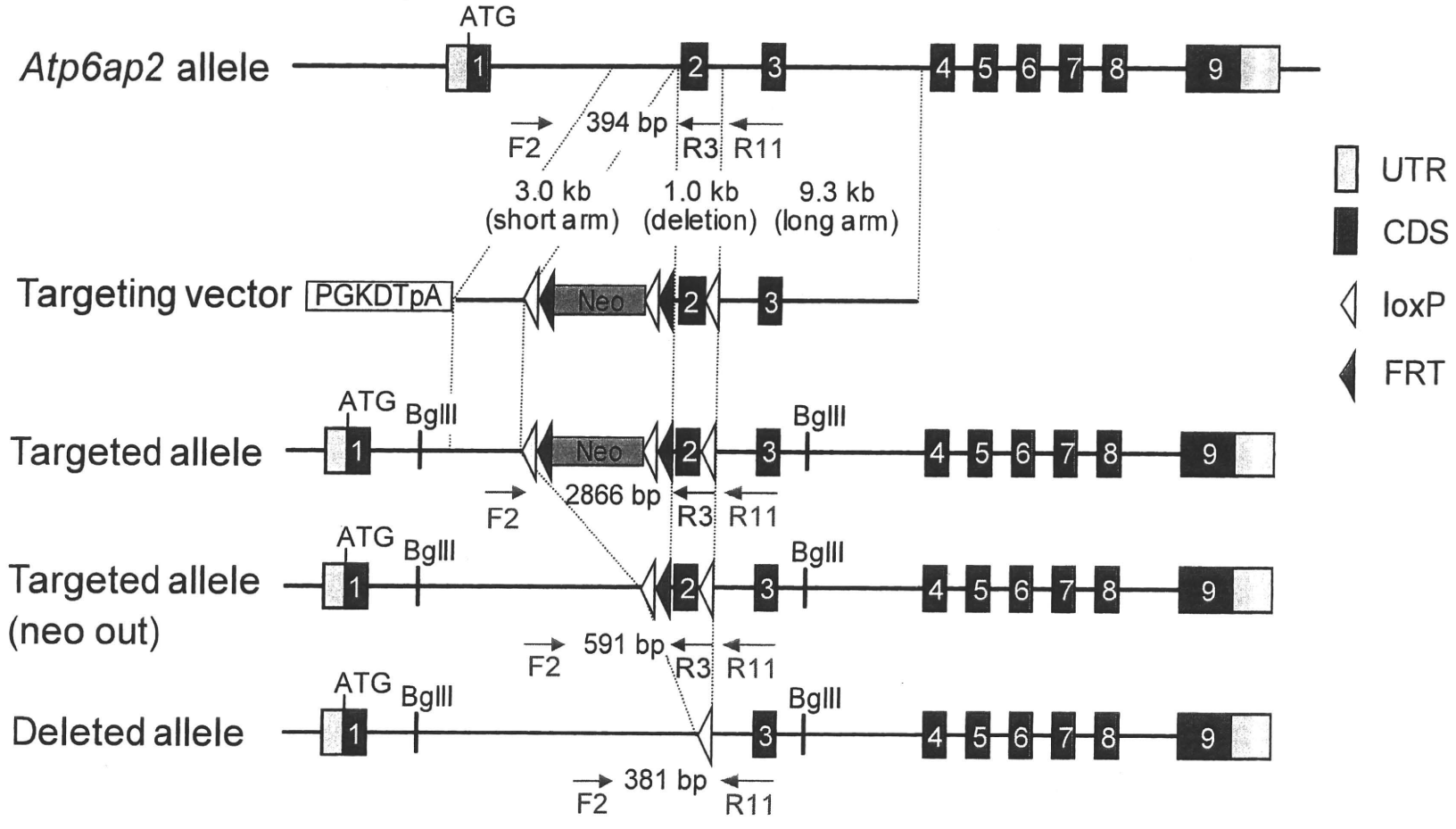

Downloaded from circres.ahajournals.org at KEIO UNIV IGAKUBU LIB on May 12, 2011

Online Figure II

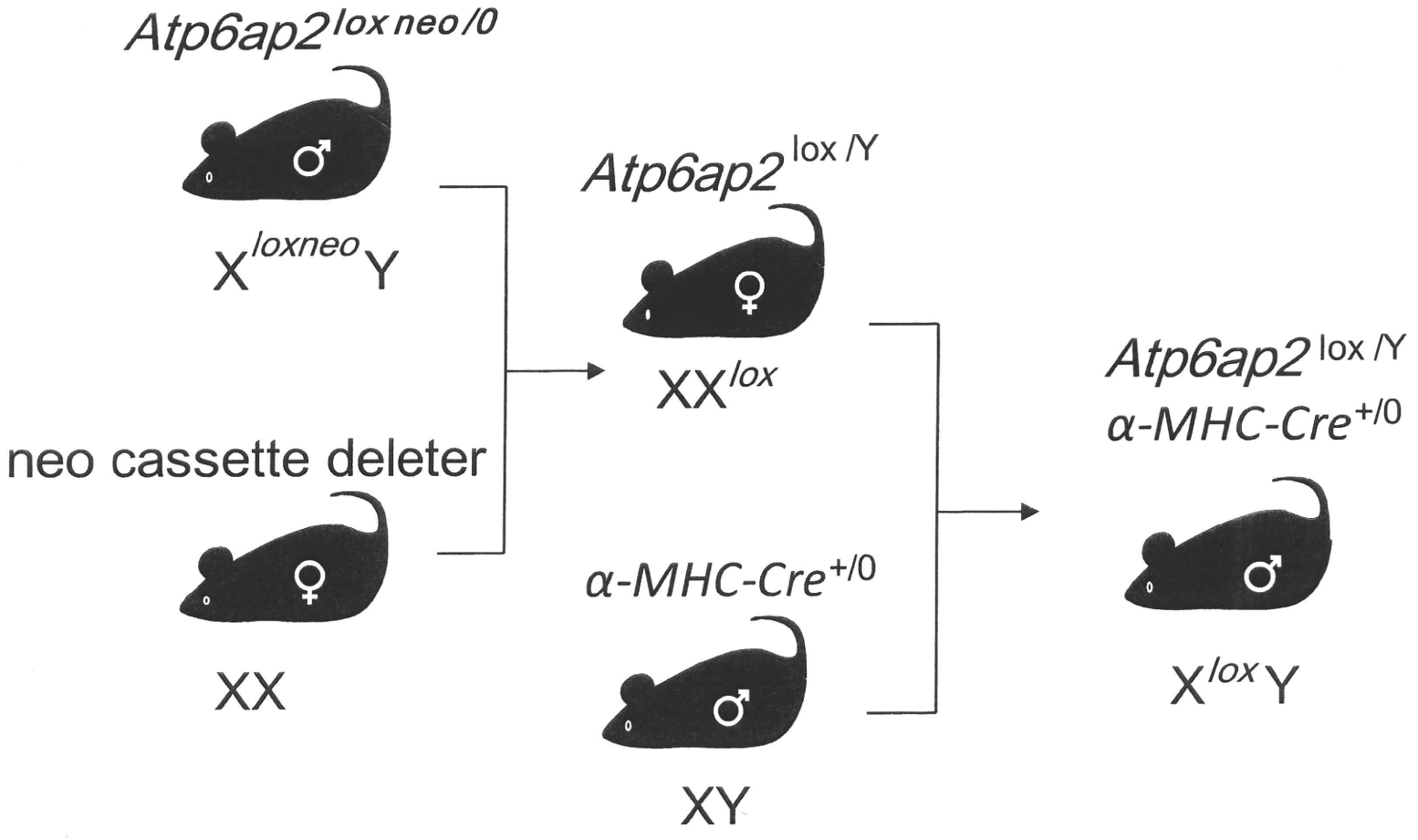

Downloaded from circres.ahajournals.org at KEIO UNIV IGAKUBU LIB on May 12, 2011

Online Figure III

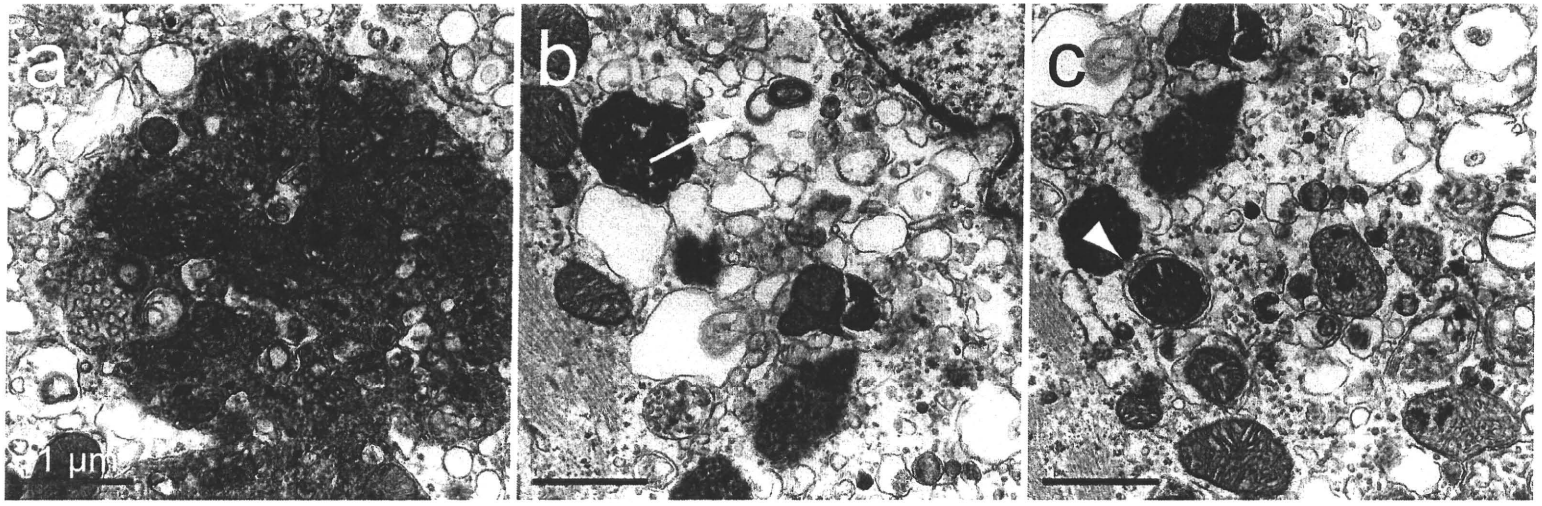

Downloaded from circres.ahajournals.org at KEIO UNIV IGAKUBU LIB on May 12, 2011

Online Figure IV

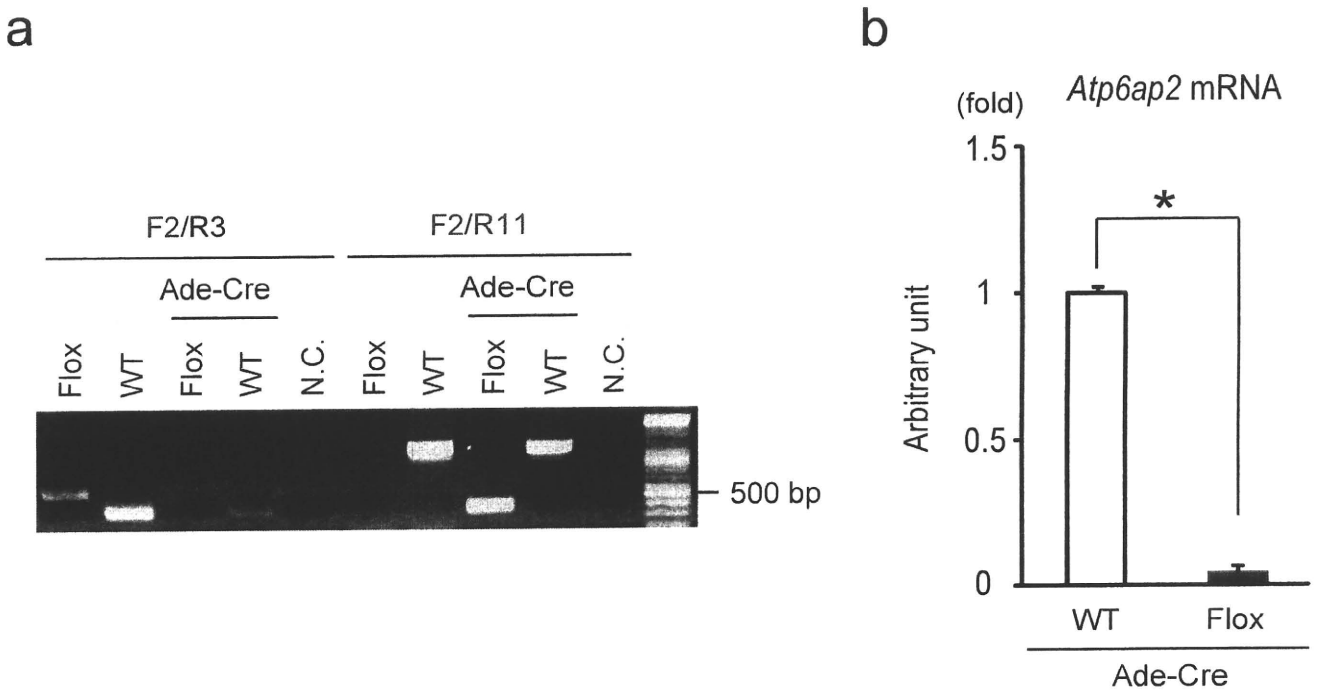

Downloaded from circres.ahajournals.org at KEIO UNIV IGAKUBU LIB on May 12, 2011

Online Figure V

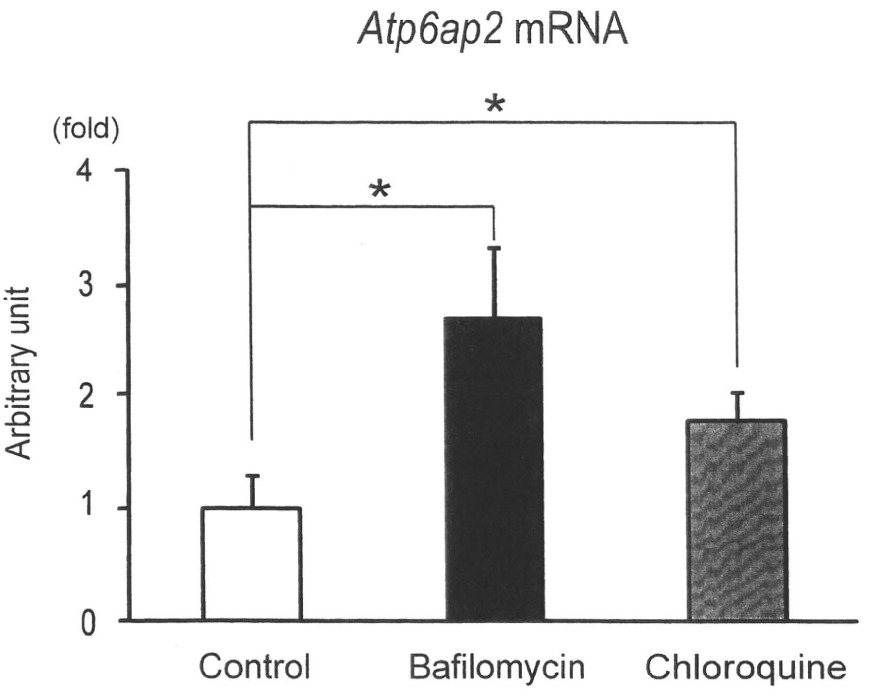

Downloaded from circres.ahajournals.org at KEIO UNIV IGAKUBU LIB on May 12, 2011

Generation of Induced Pluripotent Stem Cells from Human Terminally Differentiated Circulating T Cells

Tomohisa Seki,[1,7] Shinsuke Yuasa,[1,2,7] Mayumi Oda,[2] Toru Egashira,[1] Kojiro Yae,[1] Dai Kusumoto,[1] Hikari Nakata,[1] Shugo Tohyama,[1] Hisayuki Hashimoto,[1] Masaki Kodaira,[1] Yohei Okada,[2,3] Hiroyuki Seimiya,[4] Noemi Fusaki,[5,6] Mamoru Hasegawa,[5] and Keiichi Fukuda[1,*]

[1]Department of Cardiology
[2]Center for Integrated Medical Research
[3]Department of Physiology
Keio University School of Medicine, Tokyo 160-8582, Japan
[4]Division of Molecular Biotherapy, Cancer Chemotherapy Center, Japanese Foundation for Cancer Research, Tokyo 135-8550, Japan
[5]DNAVEC Corporation, Ibaraki 1-25-11, Japan
[6]PRESTO, JST, Saitama 332-0012, Japan
[7]These authors contributed equally to this work
*Correspondence: kfukuda@sc.itc.keio.ac.jp
DOI 10.1016/j.stem.2010.06.003

The direct reprogramming of somatic cells to produce induced pluripotent stem cells (iPSCs) is a prominent recent advance in stem cell biology (Takahashi and Yamanaka, 2006). Generation of iPSCs without genomic integration of extrinsic genes is highly desirable. Initially, human dermal fibroblasts were used to derive human iPSCs (hiPSCs) (Takahashi et al., 2007; Yu et al., 2007). However, recent studies have shown that other human somatic stem cells can be used (Aasen et al., 2008; Eminli et al., 2009; Kim et al., 2009; Ye et al., 2009). It is difficult to obtain human somatic stem cells, but human terminally differentiated circulating T cells (hTDCTCs) are readily available from peripheral blood. Here, we show that a combination of activated T cell cultivation and a temperature-sensitive mutated Sendai virus (SeV) that encodes human OCT3/4, SOX2, KLF4, and c-MYC allows the generation of hiPSCs easily, efficiently, and safely within a 1 month time frame.

Sampling of peripheral blood is one of the least invasive procedures performed routinely in clinics, and surplus peripheral blood samples are often left unused after clinical examinations. Among peripheral blood mononuclear cells (PBMCs), T cells can be readily cultured in vitro by means of a plate-bound anti-CD3 monoclonal antibody and recombinant (r)IL-2 (Desai-Mehta et al., 1996), and we used such an approach to expand hTDCTCs from peripheral blood samples. From 1 ml of whole blood, PBMCs were separated on a Ficoll gradient and then cultured with plate-bound anti-CD3 monoclonal antibody and rIL-2 (Figure 1A). Although PBMC fractions contain lymphocytes and monocytes, T cells are selectively cultured under these conditions. In culture, the number of activated T cells increased gradually but consistently. Five days after blood sampling, the cultured cells were morphologically identical to pure CD3-positive T cells collected by fluorescence-activated cell sorting (FACS) (Figure 1B). We used a whole-PBMC culture method because it is technically simpler than FACS, in which the sorted cells are frequently damaged by laser emission and the process of single-cell sorting.

To avoid transgene integration during iPSC generation, we used an SeV vector, which is a minus-strand RNA virus that is not integrated into the host genome and is not pathogenic for humans (Li et al., 2000). We used a temperature-sensitive mutated SeV vector in these experiments to reduce transgene expression and SeV residue in generated lines. This form of SeV vector generates weaker transgene expression and cannot proliferate at standard culture temperatures (data not shown). SeV can be efficiently transduced into human T cells and can express exogenous genes (Okano et al., 2003). We first introduced green fluorescent protein (GFP) into human T cells by SeV in a dose-dependent manner; toxicity for the infected cells was minimal at the virus dosages used (Figure 1C). To generate iPSCs from hTDCTCs, we used SeV to deliver multiple transgenes that encoded stem cell-specific transcription factors, such as *OCT3/4*, *SOX2*, *KLF4*, and *c-MYC*, into cells on day 6 of culture. Two days after gene introduction, the cells were replated onto feeder layers of SNL cells. On day 9, the cells were transferred to human ES cell (ESC) medium that contained 4 ng/ml bFGF. Within 3 weeks of infection, we identified a colony that resembled human ESCs (hESCs) among the T cell derivatives. On day 25, colonies that were larger and morphologically similar to hESC-like colonies were picked (Figure 1D). Of these initial colonies, which were identified by crystal violet staining, most were positive for alkaline phosphatase (ALP), which is a characteristic marker of stem cells (Figure 1E). T cells that had been transfected with SeV vectors carrying *OCT3/4, SOX2, KLF4,* and *c-MYC* were plated onto mitomycin C-treated SNL feeder cells at 5×10^4 cells per 10 cm dish. Around day 25 after blood sampling, the number of ALP-positive hESC-like colonies was counted and approximately 50 colonies were observed at MOI 20 (Figure 1E) (an efficiency of 0.1%). Moreover, the efficiency of iPSC colony generation was dependent upon the dosage of virus used for gene introduction (Figure 1F). We named these established T cell-derived iPSCs as "TiPS cells (TiPSCs)." After expansion, the cloned TiPSCs displayed typical hESC/iPSC morphology and had a normal karyotype (Figures S1A and S1B available online).

To confirm that the TiPSCs had the characteristics of typical ESC/iPSCs, we

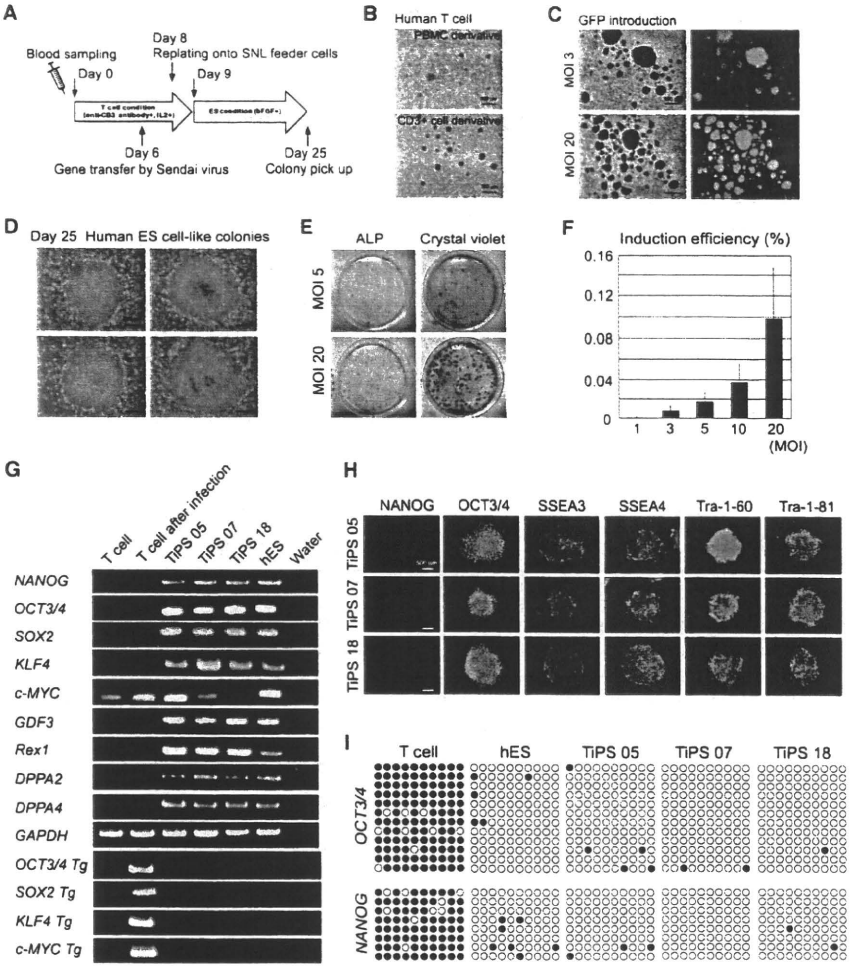

Figure 1. hTDCTCs-Derived iPSC Colonies

(A) Strategy used in the present study for reprogramming T cells.

(B) Morphologies of T cells derived from whole PBMCs or FACS-sorted T cells grown in the presence of CD3 antibody and rIL2.

(C) Efficient GFP introduction by SeV in T cells transfected at an MOI of 3 or MOI of 20.

(D) Typical ESC-like iPSC colonies on day 25 after blood sampling.

(E) Examples of 10 cm dishes stained for ALP on day 25, showing numerous ALP-positive colonies of T cells that were transfected at an MOI of 5 or MOI of 20.

(F) Numbers of ALP-positive colonies in relation to multiplicity of infection.

(G) RT-PCR analyses for the hESC marker genes *NANOG*, *OCT3/4*, *SOX2*, *KLF4*, *c-MYC*, *GDF3*, *REX1*, *DPPA2*, and *DPPA4* and the transgenes *OCT3/4*, *SOX2*, *KLF4*, and *c-MYC*.

(H) Immunofluorescence staining for pluripotency and surface markers (NANOG, OCT3/4, SSEA3, SSEA4, TRA-1-60, and TRA-1-81) in TiPS 05, 07, and 18. Scale bars represent 500 μm.

(I) Bisulfite sequencing analysis of the *NANOG* and *OCT3/4* promoter regions in peripheral T cells, hESCs, and hTiPSCs 05, 07, and 18. Each row of circles for a given amplicon represents the methylation status of the CpG dinucleotides in one bacterial clone for that region. Open circles represent unmethylated CpGs; closed circles represent methylated CpGs.

See also Figure S1 and Table S1.

examined stem cell marker expression. Reverse-transcription PCR (RT-PCR) analyses revealed that the TiPS 05, 07, and 18 clones expressed ESC marker transcripts for *NANOG*, *OCT3/4*, *SOX2*, *KLF4*, *c-MYC*, *GDF3*, *REX1*, *DPPA2*, and *DPPA4*. The original T cells also expressed *c-MYC* at a basal level, as previously reported (Douglas et al., 2001). In the TiPSCs, the *OCT3/4*, *SOX2*, *KLF4*, and *c-MYC* transgenes were lost after several passages (Figure 1G; Figure S1C). Immunostaining revealed that the TiPSCs expressed the Nanog, Oct3/4, SSEA3, SSEA4, Tra-1-60, and Tra-1-81 proteins (Figure 1H). High telomerase activity is also an important characteristic of iPSCs, and, appropriately, TiPSCs showed high levels of telomerase activity (Figure S1D). Another signature of iPSCs is epigenetic remodeling. We used bisulfite sequencing to examine the methylation status of the *NANOG* and *OCT3/4* promoters. T cells, which do not express *NANOG* or *OCT3/4*, showed mostly methylated CpGs in those promoters. hESCs, which do express *NANOG* and *OCT3/4*, showed unmethylated CpGs in those promoters. As in hESCs, the CpGs in these promoter regions were predominantly unmethylated in the TiPSCs (Figure 1I). These results suggest that SeV-mediated gene transfer successfully reprograms hTDCTCs.

Somatic recombination of T cell receptor (TCR) genes generates a diverse T cell repertoire that allows adaptation for antigen responses (Krangel, 2009). To confirm that the TiPSCs were derived from hTDCTCs, we analyzed TCR rearrangements. A hallmark of the TCR-β locus is developmentally ordered recombination, with Dβ-to-Jβ recombination preceding Vβ-to-DβJβ recombination. We performed capillary electrophoresis of the PCR products for the genomic DNA of the TCR-β regions. As a positive control, we used monoclonal T cells, which are derived from patients with lymphocyte malignancies and show a specific peak, because these T cells have only a single genetic variation in their TCR regions (Figure S2A). Peripheral T cells from people without lymphocytic diseases are polyclonal, with diverse genetic variations in their TCR rearrangements, and show a broad and low band without a specific peak. ESCs do not have TCR rearrangements and do not show a specific positive peak. The TiPS 05, 07, and 18 cell lines showed specific peaks for Dβ/Jβ recombination. TiPS 05 showed Vβ/Jβ2 recombination. TiPS 07 and TiPS 18 showed Vβ/Jβ1,2 recombination, albeit with different bands (Figure 2A). TCR rearrangement is specific for T cell development, so these results confirm that TiPSCs are derived from T cells. They also indicate that the TiPS 05, 07, and 18 lines originated from different T cells. We analyzed the rearrangement pattern of 10 independent TiPSCs and confirmed that every TiPSCs showed different rearrangement pattern (Figure S2A).

We also performed global gene expression analyses with DNA chips. Scatter plot analyses revealed global gene

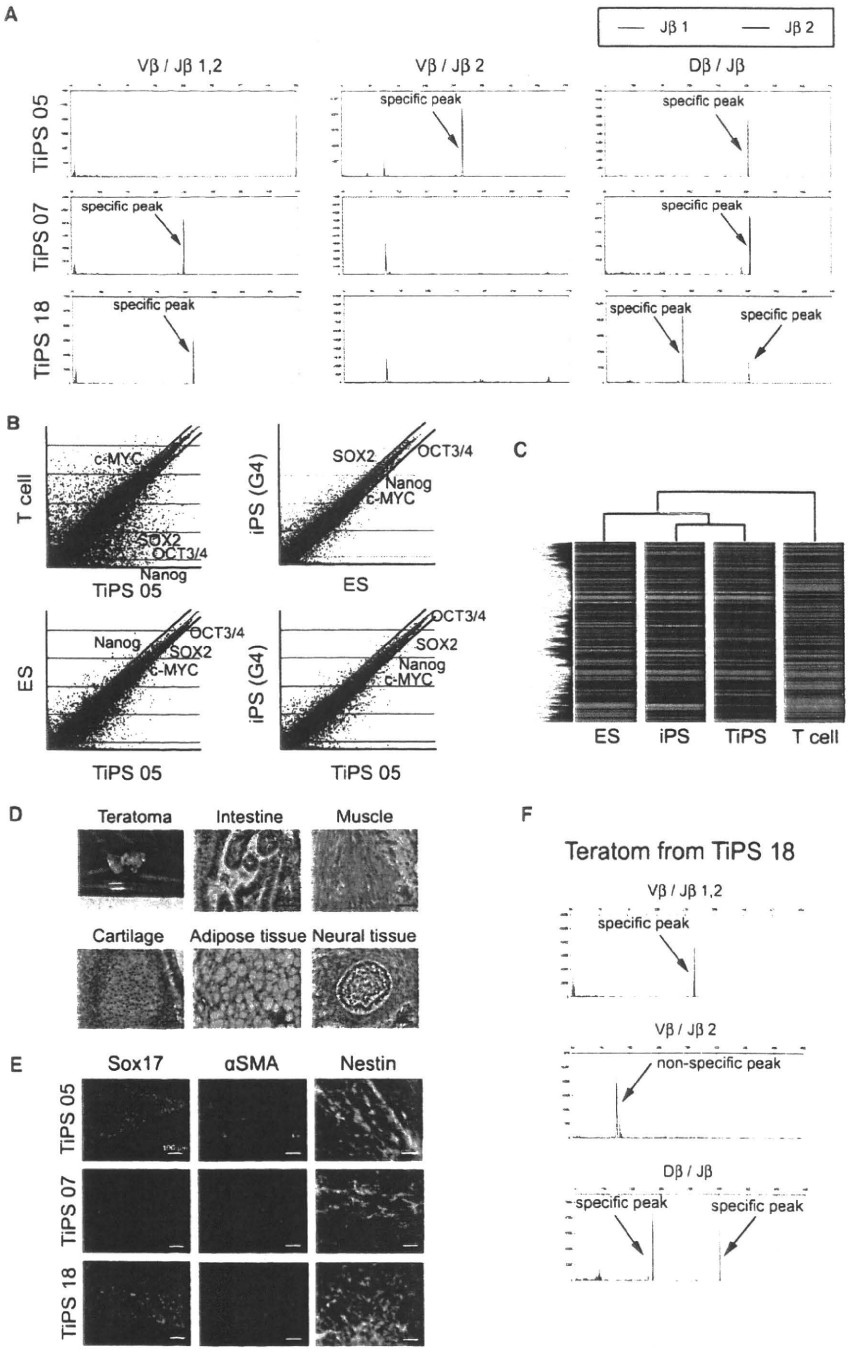

Figure 2. Detail Characterizations of TiPSCs

(A) Characterization of the TCR-β rearrangement by capillary electrophoresis. The green line is derived from the band for the Jβ1 gene, and blue line is derived from the band for the Jβ2 gene. TiPS 05 shows rearrangements of Vβ/Jβ2 and Dβ/Jβ. TiPS 07 shows rearrangements of Vβ/Jβ1,2 and Dβ/Jβ. TiPS 18 shows rearrangements of Vβ/Jβ1,2 and Dβ/Jβ.

(B) Scatter plots comparing the global gene expression profiles of T cells and TiPS cells, dermal fibroblast-derived iPSCs (G4) and ESCs, ESCs and TiPSCs, and dermal fibroblast-derived iPSCs (G4) and TiPSCs. The black lines indicate 2-fold differences in gene expression levels between the paired cell populations. The transcript expression levels are shown on a $\log_2$ scale. The expression levels of *NANOG*, *OCT3/4*, *SOX2*, and *c-MYC* are shown.

(C) Heat map analyses of hESCs, dermal fibroblast-derived iPSCs, TiPSCs, and the parental human T cells.

(D) Gross morphology, hematoxylin and eosin-stained representative teratomas derived from TiPS 05.

(E) Immunofluorescence staining for Sox17 (endodermal marker), αSMA (mesodermal marker), and Nestin (ectodermal marker) in each TiPSC-derived differentiated cell.

(F) Characterization of the TCR-β rearrangement for teratoma from TiPS 18.

See also Figure S2 and Table S2.

expression differences between peripheral T cells and TiPSCs. Comparison of hESCs and human dermal fibroblast-derived iPSCs, hESCs, and human TiPSCs (hTiPSCs), and dermal fibroblast-derived iPSCs and TiPSCs showed high levels of similarity (Figure 2B). Heat map analysis showed that the global gene expression profiles were overall similar in ESCs, dermal fibroblast-derived iPSCs, and TiPSCs, and different from T cells (Figure 2C). To further demonstrate the pluripotency of hTiPSCs, they were transplanted into the subcutaneous tissue of severe combined immunodeficient (SCID) mice. Six to eight weeks after injection, each TiPSC line tested gave rise to teratomas that contained derivatives of all three germ layers (Figure 2D; Figure S2B). We also examined the in vitro differentiation potential of TiPSCs. Each TiPSC line tested generated embryoid bodies that contained derivatives of all three germ layers (Figure 2E). These results indicate that hTiPSCs are pluripotent stem cells. Although it was reported that Trp53 null murine T cells could be reprogrammed into iPSCs (Hong et al., 2009), we have successfully reprogrammed wild-type human T cells. In our hands, the efficiency of conventional retrovirus-mediated gene transfer into wild-type human T cells was very low compared to SeV (data not shown). In our view, the efficiency of gene transfer is a major determining factor in successful iPSC generation.

With current technology, if iPSC-derived mature cells are transplanted into diseased patients, there is no good procedure for following their progeny, which could eventually form malignant or benign tumors. In animal models, several marker genes can be used to chart the progression and consequences of iPSC-derived mature cell transplantation, such as GFP and luciferase. However, it is not desirable to insert exogenous marker genes into the genomes of hiPSCs for clinical use. TiPSCs, however, already have a traceable genetic signature through TCR locus rearrangement. Consistent with this idea, teratomas derived from TiPSCs had

same signature as undifferentiated TiPSCs (Figure 2F; Figure S2C). Therefore, the descendents of TiPSCs can be identified by analyzing their TCR rearrangement patterns.

In conclusion, we have developed a minimally invasive method for hiPSC generation without genomic integration that uses low numbers of hTDCTCs from peripheral blood. This method has advantages for research into stem cell reprogramming, TCR rearrangement, immunologic disorders, and the development of genetic markers for future applications of regenerative medicine. TiPSCs may well be relatively easy to use in a clinical setting.

ACCESSION NUMBERS

The microarray data have been deposited in GEO and given the series accession number GSE22088.

SUPPLEMENTAL INFORMATION

Supplemental Information includes Supplemental Experimental Procedures, two figures, and two tables and can be found with this article online at doi:10.1016/j.stem.2010.06.003.

ACKNOWLEDGMENTS

This study was supported in part by research grants from the project for realization of regenerative medicine, the Ministry of Education, Science, and Culture, Japan, and by a grant from the New Energy and Industrial Technology Development Organization (NEDO). We thank Dr. Kyotaro Hirashima for technical assistance with TRAP assay. N.F. is an employee of DNAVEC Corporation and M.H. is a founder and shareholder of DNAVEC Corporation

Received: May 5, 2010
Revised: June 3, 2010
Accepted: June 5, 2010
Published: July 1, 2010

REFERENCES

Aasen, T., Raya, A., Barrero, M.J., Garreta, E., Consiglio, A., Gonzalez, F., Vassena, R., Bilic, J., Pekarik, V., Tiscornia, G., et al. (2008). Nat. Biotechnol. *26*, 1276–1284.

Desai-Mehta, A., Lu, L., Ramsey-Goldman, R., and Datta, S.K. (1996). J. Clin. Invest. *97*, 2063–2073.

Douglas, N.C., Jacobs, H., Bothwell, A.L., and Hayday, A.C. (2001). Nat. Immunol. *2*, 307–315.

Eminli, S., Foudi, A., Stadtfeld, M., Maherali, N., Ahfeldt, T., Mostoslavsky, G., Hock, H., and Hochedlinger, K. (2009). Nat. Genet. *41*, 968–976.

Hong, H., Takahashi, K., Ichisaka, T., Aoi, T., Kanagawa, O., Nakagawa, M., Okita, K., and Yamanaka, S. (2009). Nature *460*, 1132–1135.

Kim, J.B., Greber, B., Arauzo-Bravo, M.J., Meyer, J., Park, K.I., Zaehres, H., and Scholer, H.R. (2009). Nature *461*, 649–653.

Krangel, M.S. (2009). Curr. Opin. Immunol. *21*, 133–139.

Li, H.-O., Zhu, Y.-F., Asakawa, M., Kuma, H., Hirata, T., Ueda, Y., Lee, Y.-S., Fukumura, M., Iida, A., Kato, A., et al. (2000). J. Virol. *74*, 6564–6569.

Okano, S., Yonemitsu, Y., Nagata, S., Sata, S., Onimaru, M., Nakagawa, K., Tomita, Y., Kishihara, K., Hashimoto, S., Nakashima, Y., et al. (2003). Gene Ther. *10*, 1381–1391.

Takahashi, K., and Yamanaka, S. (2006). Cell *126*, 663–676.

Takahashi, K., Tanabe, K., Ohnuki, M., Narita, M., Ichisaka, T., Tomoda, K., and Yamanaka, S. (2007). Cell *131*, 861–872.

Ye, Z., Zhan, H., Mali, P., Dowey, S., Williams, D.M., Jang, Y.-Y., Dang, C.V., Spivak, J.L., Moliterno, A.R., and Cheng, L. (2009). Blood *114*, 5473–5480.

Yu, J., Vodyanik, M.A., Smuga-Otto, K., Antosiewicz-Bourget, J., Frane, J.L., Tian, S., Nie, J., Jonsdottir, G.A., Ruotti, V., Stewart, R., et al. (2007). Science *318*, 1917–1920.

Note Added in Proof

A manuscript has appeared online demonstrating isolation of iPSCs from peripheral blood, including a single line that showed evidence for both TCR-β and TCR-γ rearrangement by PCR (Kunisato, A., Wakatsuki, M., Shinba, H., Ota, T., Ishida, I., and Nagao, K. [2010]. Direct generation of induced pluripotent stem cells from human non-mobilized blood. Stem Cells Dev., in press. Published online May 24, 2010. 10.1089/scd.2010.0063).

Periostin advances atherosclerotic and rheumatic cardiac valve degeneration by inducing angiogenesis and MMP production in humans and rodents

Daihiko Hakuno,[1,2] Naritaka Kimura,[1,3] Masatoyo Yoshioka,[1] Makio Mukai,[4] Tokuhiro Kimura,[5] Yasunori Okada,[5] Ryohei Yozu,[3] Chisa Shukunami,[6] Yuji Hiraki,[6] Akira Kudo,[7] Satoshi Ogawa,[2] and Keiichi Fukuda[1]

[1]Department of Regenerative Medicine and Advanced Cardiac Therapeutics, [2]Cardiology Division, Department of Internal Medicine, [3]Department of Cardiovascular Surgery, [4]Division of Diagnostic Pathology, [5]Department of Pathology, Keio University School of Medicine, Tokyo, Japan. [6]Department of Cellular Differentiation, Institute for Frontier Medical Sciences, Kyoto University, Kyoto, Japan. [7]Department of Biological Information, Tokyo Institute of Technology, Kanagawa, Japan.

Valvular heart disease (VHD) is the term given to any disease process involving one or more of the heart valves. The condition can be congenital or acquired, for example as a result of atherosclerosis or rheumatic fever. Despite its clinical importance, the molecular mechanisms underlying VHD remain unknown. We investigated the pathophysiologic role and molecular mechanism of periostin, a protein that plays critical roles in cardiac valve development, in degenerative VHD. Unexpectedly, we found that periostin levels were drastically increased in infiltrated inflammatory cells and myofibroblasts in areas of angiogenesis in human atherosclerotic and rheumatic VHD, whereas periostin was localized to the subendothelial layer in normal valves. The expression patterns of periostin and chondromodulin I, an angioinhibitory factor that maintains cardiac valvular function, were mutually exclusive. In WT mice, a high-fat diet markedly increased aortic valve thickening, annular fibrosis, and MMP-2 and MMP-13 expression levels, concomitant with increased periostin expression; these changes were attenuated in periostin-knockout mice. In vitro and ex vivo studies revealed that periostin promoted tube formation and mobilization of ECs. Furthermore, periostin prominently increased MMP secretion from cultured valvular interstitial cells, ECs, and macrophages in a cell type–specific manner. These findings indicate that, in contrast to chondromodulin I, periostin plays an essential role in the progression of cardiac valve complex degeneration by inducing angiogenesis and MMP production.

Introduction

The prevalence of valvular heart disease (VHD) increases with age, reaching 13% in individuals 75 years of age or older (1). The morbidity associated with degenerative aortic valve disease is of global interest, given the aging of populations worldwide and the habitual consumption of food high in calories and cholesterol. Several lines of evidence (2–5) suggest that the mechanism of aortic valve degeneration is similar to that of atherosclerosis, namely, infiltration of inflammatory cells and accumulation of oxidized LDL within the valve, proliferation of valvular interstitial cells (VICs), extracellular matrix remodeling, and calcification. Based on this mechanism, prospective, randomized clinical trials of HMG CoA reductase inhibitors for preventing the progression of aortic valve stenosis have been performed, although the results are controversial (6, 7). As no preventive pharmacologic therapy for degenerative VHD has been proposed to date, further investigations into the underlying disease mechanisms and the development of novel therapies are warranted.

The previous studies conducted on VHD have largely been observational, immunohistologic, and in vitro studies (8–13). Although the onset of aortic valve stenosis has been reported in Smad6-deficient mice (14), in fibulin 4–deficient mice (15), and in humans with the *NOTCH1* mutation (16), the abnormality has primarily been observed during cardiac valve development. As avascular tissues, the cardiac valve complex and cartilage share common structural properties (17, 18). The cartilage and tendons are known to have unique angioinhibitory mechanisms (19), disruption of which results in angiogenesis and destruction of the joint, leading to arthritis (20). In contrast, angiogenesis and VEGF expression are increased in calcified aortic valves (21, 22). Previously, we showed that chondromodulin I (encoded by *Lect1*) and tenomodulin, angioinhibitory factors expressed in the cartilage and tendon, respectively, were expressed in the cardiac valves and chordae tendineae cordis (23, 24), respectively. Whereas chondromodulin I was expressed in the normal cardiac valves, its expression was diminished in areas of angiogenesis in the degenerated valves of human VHD. The absence of chondromodulin I results in angiogenesis and early stage aortic valve stenosis in mice, which indicates that cardiac valve degeneration is promoted by pathologic angiogenesis. The focal absence of tenomodulin is associated with angiogenesis and rupture of the chordae tendineae cordis.

Periostin (encoded by *Postn*) is a TGF-β–inducible, 90-kDa, secreted protein originally identified in mouse osteoblasts, in which it promotes adhesion and migration (25, 26). Periostin is detected as spliced isoforms and contains 4 repeats of the fasciclin domain, which shares homology with the *Drosophila* protein fasciclin I involved in neuronal cell-cell adhesion (27). In addition to

Conflict of interest: The authors have declared that no conflict of interest exists.

Citation for this article: *J Clin Invest.* 2010;120(7):2292–2306. doi:10.1172/JCI40973.

the periosteum and periodontal ligament, periostin is expressed in cancer cells, vascular smooth muscle cells, fibroblasts, and wound-site blood vessels and participates in tumor angiogenesis, metastasis, and cell migration (28–31). In the heart, periostin is physiologically expressed in embryonic cardiac valves, while it is reexpressed abundantly in adult LV after pressure overload or myocardial infarction (32–37). Although heart size and cardiomyocyte number are unchanged at baseline in *Postn*$^{-/-}$ mice, LV remodeling and hypertrophy are attenuated without apparently affecting the proliferation of cardiomyocytes and cardiac fibroblasts, which suggests crucial effects of periostin on LV fibrosis and hypertrophy after cardiac insult (34, 35). Previous studies have clearly demonstrated the physiologic role of periostin in the cardiac valve and its critical involvement in cardiac valve maturation during development (38, 39). However, it remains unknown whether periostin plays any pathophysiologic role in adult valvular function.

During our investigation of degenerated human cardiac valves, we unexpectedly found that periostin was strikingly increased in patients with atherosclerotic and rheumatic VHD. This finding led us to hypothesize that periostin plays a distinct pathophysiologic role in degenerated cardiac valves. The present study demonstrates, for the first time to our knowledge, the involvement of periostin in the process of cardiac valve complex degeneration using human surgical specimens. We also investigated the pathophysiologic role of periostin in VHD using high-fat (HF) diet–induced degeneration of the cardiac valve complex and its rescue in *Postn*$^{-/-}$ mice. We further clarified the molecular mechanism by analyzing the in vitro effects of periostin on ECs, VICs, and engrafted macrophages.

Results

Periostin isoforms are specifically expressed in the cardiac valves and annuli of rodent hearts from the embryonic stage to adulthood. Because murine periostin is known to have 4 spliced isoforms within the C-terminal domain (Figure 1A, right), we initially determined the temporal and spatial expression patterns of the periostin isoforms in embryonic and adult mouse hearts. The RT-PCR analysis revealed that the periostin isoforms were first expressed in the E8.5 heart, and their levels increased thereafter (Figure 1A, left). Interestingly, the shift from the long isoform to the short isoform of periostin mRNA occurred in the postnatal heart. Western blot analysis revealed that the relative expression level of this protein in a heart decreased postnatally, probably as a result of its limited expression in valvular areas (Figure 1B). Furthermore, the short isoform was predominantly expressed in adult murine aortic valves, whereas the long isoform was mainly expressed in the mitral valves (Figure 1C).

Immunofluorescence staining with an anti-periostin antibody that recognizes both long and short isoforms showed that periostin was specifically expressed in the outflow tract and atrioventricular canal at E11.5 and in the cardiac valves and their annuli thereafter (Figure 1D). At 4 postnatal weeks, periostin expression appeared to be more localized to the subendothelial superficial layers of the cardiac valves and annuli.

Immunohistochemistry (IHC) of the adult rat cardiac valves confirmed that periostin was expressed in all 4 (aortic, mitral, pulmonary, and tricuspid) valves and in their annuli, in which the expression pattern of periostin was similar to that seen in murine valves (Figure 1E). These results indicate that periostin is expressed from E8.5 to adulthood in all 4 cardiac valves and that its expression is localized to the subendothelial superficial layers of the cardiac valves in adult rodent hearts.

Physiologic expression of periostin is localized primarily to the zona ventricularis/atrialis and zona fibrosa in adult human cardiac valves. Next, we investigated periostin expression in adult human normal cardiac valves obtained at autopsy. IHC revealed that periostin was expressed in the superficial layers of the normal aortic and mitral valves, whereas it was expressed throughout the murine embryonic valves (Figure 2, A and B, and Supplemental Figure 1; supplemental material available online with this article; doi:10.1172/JCI40973DS1). Of note, periostin was strongly expressed at the zona ventricularis side of the aortic valve and the atrialis side of the mitral valve, and to a lesser extent at the zona fibrosa of both, just beneath the ECs.

We also performed triple immunofluorescence staining for periostin and other components of the aortic valves. Interestingly, periostin was expressed in the subendothelial superficial layer, whereas chondromodulin I, an angioinhibitory protective factor in the cardiac valve (23), was expressed in the core layer of the cardiac valve (Figure 2C). Therefore, the expression patterns of these 2 proteins are mutually exclusive. The expression pattern of periostin did not coincide with that of either vWF or collagen I (Figure 2, D and E). Human cardiac valves consist of 3 distinct layers of extracellular matrix (fibrosa, spongiosa, and atrialis-ventricularis), and elastin is the predominant component of the atrialis and ventricularis (40). Indeed, the regions of periostin expression largely overlapped those of elastin (Figure 2F). Similar expression patterns were observed in the mitral valves (Supplemental Figure 2).

Periostin expression is strikingly upregulated and expanded in patients with atherosclerotic and rheumatic VHD. To investigate whether periostin is involved in the pathogenesis of VHD, we compared its expression profiles in normal human cardiac valves and in the cardiac valves of patients with VHD. Pathologic cardiac valves obtained by valvular replacement surgery, including atherosclerotic, rheumatic, and prolapse valves (n = 8, 9, and 4, respectively), were examined by IHC. Unexpectedly, we found not only that periostin expression was markedly elevated in the subendothelial superficial layer, but also that the area of periostin expression was expanded in the cardiac valves in patients with degenerative VHD, such as those with atherosclerotic or rheumatic valves. In the periostin-positive areas of the atherosclerotic valves, chondromodulin I expression was absent, whereas VEGF was upregulated and the small vessels were heavily infiltrated (Figure 3A). Similar findings were observed for rheumatic valves, whereas the periostin expression pattern did not show any significant changes in patients with mitral valve prolapse (Supplemental Figure 3).

Quantitative analysis revealed that the percentage of the expression area of periostin was increased 4.0-fold in patients with atherosclerotic and rheumatic valves, but not in those with valvular prolapse (Figure 3B). In patients with atherosclerotic or rheumatic valves, the chondromodulin I–positive areas were decreased to 25%, and the small vessel density, detected by vWF staining and VEGF expression, was markedly elevated, as we reported previously (23).

Western blot analysis revealed that the levels of periostin expression increased 6.1-fold and 3.2-fold in atherosclerotic and rheumatic VHD, respectively (Figure 3C). Concomitant with these increases in periostin, the levels of expression of α-SMA and collagen I were drastically increased in these patients.

Next, we examined the relationships between the areas of angiogenesis and periostin expression in these forms of VHD. IHC showed that neoangiogenesis occurred mainly at the zona atrialis/ventricularis and zona spongiosa in the mid-regions of the valves, especially in areas in which normal vWF expression was dimin-

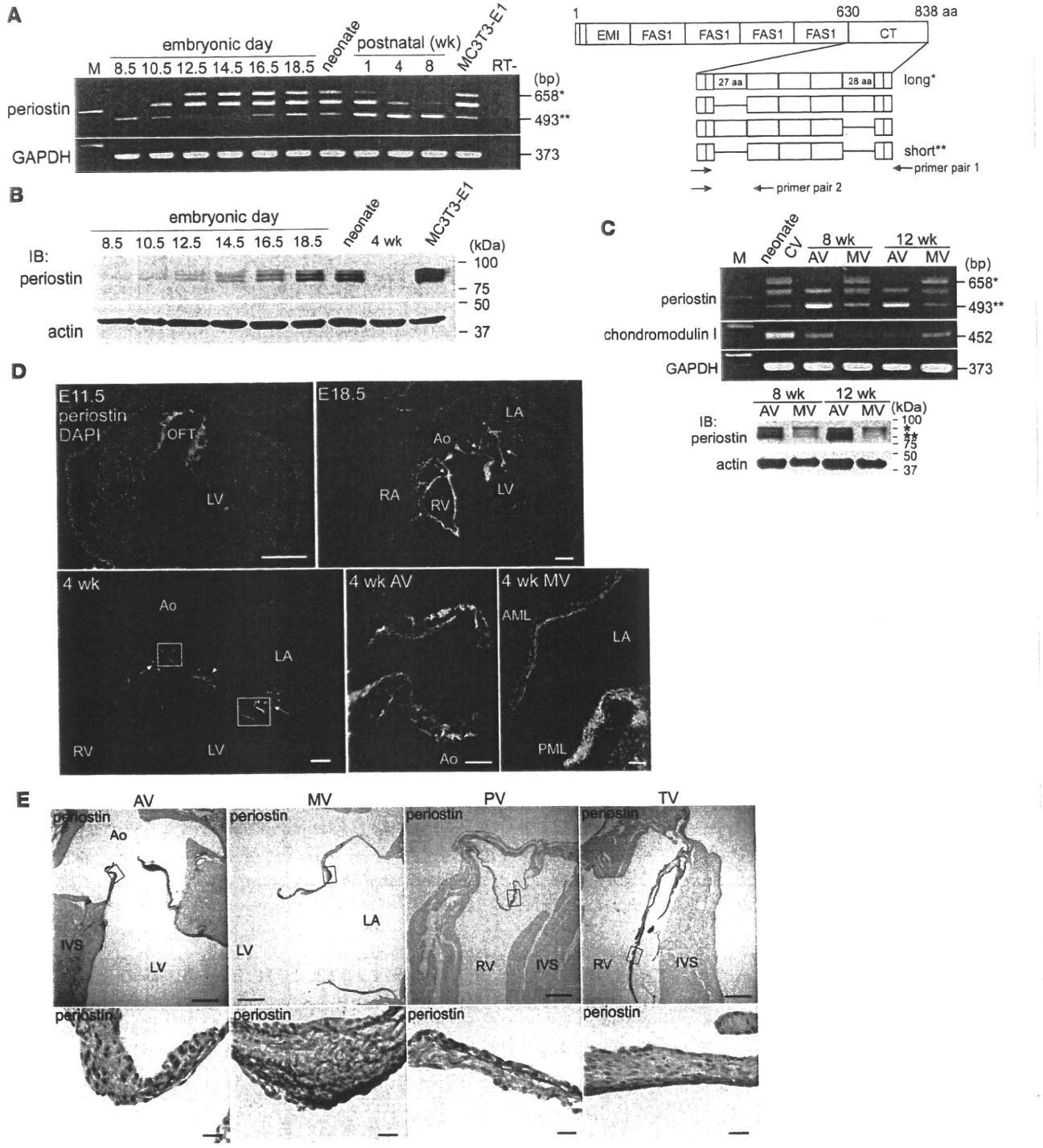

Figure 1

Periostin isoforms are specifically expressed in the cardiac valves and annuli of embryonic and adult rodent hearts. (**A** and **B**) RT-PCR (**A**) and Western blot (**B**) analyses of periostin isoforms in the mouse heart. The primer pair 1 for murine periostin (**A**, right) was used for PCR. Each box in the C-terminal (CT) domain represents an exon. Single and double asterisks represent the long and short periostin isoforms, respectively. Periostin was first detected in the hearts at E8.5, and the relative expression level of this protein decreased postnatally. MC3T3-E1 cells are a positive control. M, marker; FAS1, fasciclin I domain. (**C**) RT-PCR (top) and Western blot (bottom) analyses of the periostin isoforms in adult mouse cardiac valves (CV). AV, aortic valve; MV, mitral valve. (**D** and **E**) Immunostaining for periostin in the hearts of mice at E11.5 to 4 weeks of age (**D**) and in the heart of a 6-week-old rat (**E**). In **D**, periostin was specifically expressed in the outflow tract (OFT), cardiac valves, and annuli (arrows). In **E**, periostin (brown) was expressed in all 4 cardiac valves and their annuli. The boxed regions are shown at higher magnification. Note that periostin was localized to the subendothelial superficial layer of the adult cardiac valve. AML, anterior mitral leaflet; Ao, aorta; IVS, interventricular septum; LA, left atrium; PML, posterior mitral leaflet; PV, pulmonary valve; RA, right atrium; TV, tricuspid valve. Scale bars: 200 μm (**D**); 50 μm (**D**, higher magnification); 500 μm (**E**); 20 μm (**E**, higher magnification).

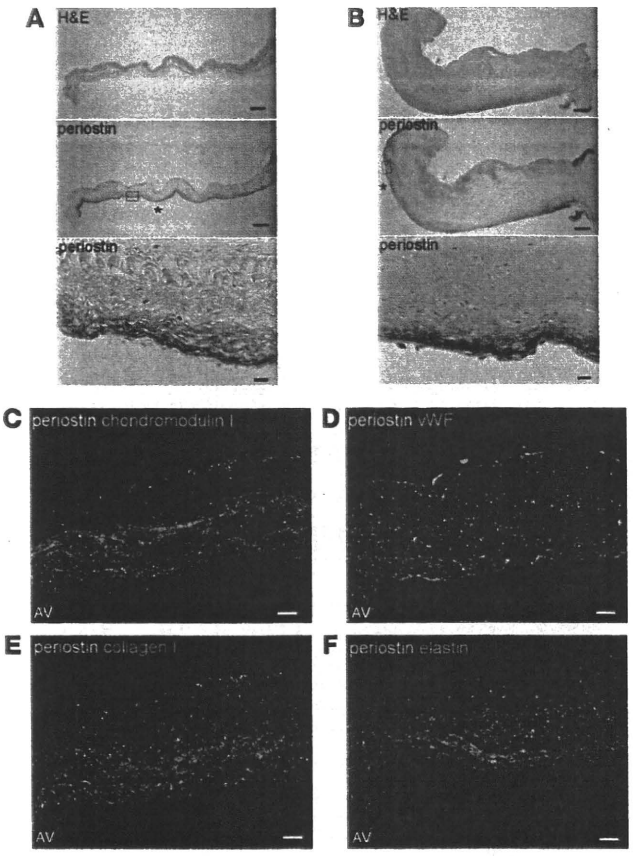

Figure 2
Physiologic expression of periostin is localized primarily to the zona ventricularis/atrialis and zona fibrosa in adult human cardiac valves. Representative, consecutive sections of normal human cardiac valves subjected to IHC (**A** and **B**) and triple-immunofluorescence staining (**C–F**). (**A** and **B**) IHC sections of the aortic valves (**A**) and mitral valves (**B**). The boxed regions in the periostin-stained sections are shown at higher magnification below. Prominent expression of periostin was observed at the ventricularis and atrialis sides (asterisks) and to a lesser extent at the zona fibrosa, just beneath the ECs. (**C–F**) Localization of periostin (green) and other components (red) in the normal aortic valves. Nuclei are stained blue. Since periostin was expressed in the subendothelial superficial layer and chondromodulin I in the core layer of the valve, the expression patterns of these proteins are mutually exclusive (**C**). The expression pattern of periostin overlapped with that of elastin (**F**), but not those of vWF and collagen I (**D** and **E**). Scale bars: 500 μm (**A** and **B**); 20 μm (**A** and **B**, higher magnification); 100 μm (**C–F**).

ished in the valve endocardium (Supplemental Figure 4A). We also found that periostin expression was specifically increased in the areas of neoangiogenesis in the degenerated valves (Supplemental Figure 4B). To identify the cell types that synthesize periostin in VHD, double immunofluorescence staining with periostin and vWF, α-SMA, vimentin, or the activated monocyte/macrophage marker CD14 was performed. Immunofluorescence staining revealed that periostin expression was increased in the interstitial tissues of the areas of angiogenesis, into which inflammatory cells and myofibroblasts had infiltrated (Figure 4A). Indeed, periostin was coexpressed with α-SMA, vimentin, and CD14 in these cells (Figure 4B). Immunofluorescence staining and Western blot analysis further confirmed that periostin was expressed and secreted from CD14-positive, cultured mouse BM-derived macrophages (Figure 4, C and D). These results indicate that periostin expression in degenerative atherosclerotic and rheumatic VHD, but not in prolapsed VHD, is completely different from its physiologic expression. In these forms of VHD, levels of periostin are markedly increased in the interstitial tissues of the newly formed small vessel areas, and periostin is secreted from the infiltrated inflammatory cells and myofibroblasts.

HF diet–induced thickening of the aortic valves and annuli is attenuated in Postn$^{-/-}$ mice. Our initial results led us to investigate whether the increased expression of periostin plays an essential role in cardiac valve degeneration or is merely an epiphenomenon. To resolve this issue, we generated *Postn*$^{-/-}$ mice of C57BL/6 strain (Figure 5A), and WT and *Postn*$^{-/-}$ mice at 12 weeks of age were fed either normal or HF diet for 4 months; C57BL/6 mice are the most atherosclerosis sensitive among mouse strains (41), and the HF regimen is known to cause significant thickening of their aortic valves, resulting in early-stage aortic valve stenosis (42). We found that the HF diet caused similar levels of obesity and hypercholesterolemia in WT and *Postn*$^{-/-}$ mice (Figure 5B).

We next performed 45-MHz echocardiography, which revealed that the HF diet produced high-echogenic areas in the aortic and mitral valve annuli in the HF diet–fed WT mice (Figure 5C). Moreover, the M-mode of echocardiography demonstrated that the aortic valve was apparently thickened in WT mice fed the HF diet compared with the normal diet. Surprisingly, the high-echogenic areas and aortic valve thickening were strongly attenuated in the HF diet–fed *Postn*$^{-/-}$ mice. Using quantitative analyses, we confirmed that the aortic valve thicknesses and echogenic areas of the annuli were significantly increased in HF diet–fed WT mice compared with WT mice fed normal diet, whereas these changes were strongly reduced in the HF diet–fed *Postn*$^{-/-}$ mice (Figure 5D). The wall thickness, internal diameter, and ejection fraction of the LV were unchanged in all the groups (Supplemental Figure 5). These results suggest that periostin is intrinsically involved in HF diet–induced degeneration of the cardiac valve complex.

HF diet–induced fibrosis and MMP expression in the cardiac valve complex are reduced in Postn$^{-/-}$ mice. To investigate further the role of periostin in valve degeneration, IHC and Western blot analysis were performed. Through quantitative analysis of the IHC sections, we confirmed that the HF diet increased the areas of periostin expression 2.2- to 2.5-fold in the aortic and mitral valve complexes of the WT mice (Figure 6, A and B). In addition, the areas of expression of vWF, collagen I, and α-SMA were increased in the HF diet–fed WT mice compared with WT mice fed normal diet, whereas expression levels of these proteins were markedly reduced in HF diet–fed *Postn*$^{-/-}$ mice.

The mitral valve complexes were then excised from the mice and subjected to Western blot analysis. The expression levels of periostin, collagen I, and α-SMA were significantly upregulated in the HF diet–fed WT mice and decreased in the HF diet–fed *Postn*$^{-/-}$ mice, confirming the IHC results (Figure 6C). It is well known that MMPs play critical roles in tissue remodeling and angiogenesis and are closely linked to the progression of atherosclerosis, aortic aneurysm, LV remodeling, and arthritis (43). Among the MMPs, MMP-13 is considered to fulfill the role of MMP-1 in rodents, which do not express the latter protein postnatally (44). Moreover, it has been reported previously that the levels of MMP-1, MMP-2, MMP-9, and MMP-13 are increased in the car-